PAPER • OPEN ACCESS

Model for access and stability of the X-point radiator and the threshold for marfes in tokamak plasmas

To cite this article: U. Stroth *et al* 2022 *Nucl. Fusion* **62** 076008

OPEN ACCESS
IOP Publishing | International Atomic Energy Agency Nuclear Fusion
Nucl. Fusion **62** (2022) 076008 (16pp) https://doi.org/10.1088/1741-4326/ac613a

Model for access and stability of the X-point radiator and the threshold for marfes in tokamak plasmas

U. Stroth[1,2,*], M. Bernert[1], D. Brida[1], M. Cavedon[3], R. Dux[1], E. Huett[1,2], T. Lunt[1], O. Pan[1], M. Wischmeier[1] and the ASDEX Upgrade Team[a]

[1] Max Planck Institute for Plasma Physics, 85748 Garching, Germany
[2] Physik-Department E28, Technische Universität München, 85747 Garching, Germany
[3] Dipartimento di Fisica G. Occhialini, Università di Milano-Bicocca, Milano, Italy

E-mail: ulrich.stroth@ipp.mpg.de

Received 13 October 2021, revised 4 March 2022
Accepted for publication 25 March 2022
Published 26 April 2022

Abstract

Based on particle and energy balances, a reduced model is derived for the physical mechanisms leading to the occurrence of stable and unstable X-point radiators (XPRs), the latter also known as marfes. The leading roles of the neutral deuterium density in the divertor region for initiating XPRs is highlighted. An access condition is formulated whose parameter dependencies are consistent with experimental observations and which could also apply to the process of divertor detachment. With an exponential increase of the recombination rate at low temperature, the XPR becomes magnetohydrodynamically unstable, leading to a marfe and, possibly, to a disruption. A critical density for marfe occurrence is formulated with the upstream density and safety factor as leading parameters, as in the experiment. Marfes are predicted to be more likely in carbon devices than in impurity-seeded plasmas in tungsten devices. The edge plasma parameter domain where marfes occur resembles that used for active marfe avoidance schemes. Both the XPR and marfe occurrence parameter can be used to guide active discharge control.

Keywords: exhaust, X-point radiator, divertor detachment, marfe, disruption control

(Some figures may appear in colour only in the online journal)

1. Introduction

High-density ($>10^{20}$ m^{-3}), low-temperature (<10 eV) plasma volumes play an important role in power exhaust and the protection of the plasma facing components of fusion devices. This work deals with generation and stability of such a plasma volume called an X-point radiator (XPR). They occur on closed magnetic flux surfaces near the magnetic X-point in diverted tokamak plasmas. Herein, an analytical model is presented and analysed with the aim of identifying the physical mechanisms and parameters that lead to the formation of XPRs and to their instability causing them to become a moving marfe[4]. In a fusion reactor, both the XPR and the marfe must be actively controlled, the former to maintain a detached divertor and the latter to avoid disrupting the tokamak discharge. By identifying critical parameters for the two phenomena, an improved understanding is developed of the working principles of the control schemes that are in development.

Cold, dense and strongly radiating plasma volumes were observed in limited [2, 3] and diverted tokamak discharges [4]

* Author to whom any correspondence should be addressed.

[a] See U. Stroth et al 2021 (https://doi.org/10.1088/1741-4326/ac207f) for the ASDEX Upgrade Team.

[4] Multifaceted asymmetric radiation from the edge [1].

since the early days of fusion research. They were dubbed marfes [1] and arise from local cooling of the plasma by interaction with neutral hydrogen and impurities. A causal relationship between this plasma cooling, the consequent tokamak density limit [5] and harmful disruptions was also established early on [6, 7].

A typical theoretical marfe model is based on a power balance where the thermal instability related to impurity radiation plays the key role in obtaining a cold plasma [1, 4, 8–10]. In general, early models developed for ohmically heated plasmas reproduce experimentally observed parameter dependencies of marfe formation, such as a density threshold that increases with plasma current and decreases with impurity concentration [1, 3].

In present day experiments, and for future reactors, dense plasma volumes play a major role in obtaining what is projected to be an obligatory detached plasma state [11, 12]. They appear close to the divertor targets or, in an extended form, as a *density front* in the high-field-side scrape-off layer (SOL) [12]. They also occur within the separatrix above the magnetic X-point, where they were observed as *X-point marfes* in the carbon devices AUG (AUG) [7], DIII-D [11] and JT-60U [13] or as XPRs in the metal walled devices AUG [14] and JET [15–17], where, in absence of carbon, nitrogen, neon or argon is injected into the plasma to increase radiative cooling. Temperatures in the 1 eV range and densities close to 10^{21} m^{-3} have been measured on JT-60U [18] and on AUG [19, 20] above the X-point in lower single null configurations. While marfes are generally unstable, trigger disruptions and define the density limit [21], the XPR is a stable and actively controllable phenomenon which has become an important element of divertor detachment control [19]. Recently, a plasma solution that included an XPR was recovered in an SOLPS-ITER transport code [22] simulation based on an AUG H-mode discharge [23]. In the simulation, up to 90 % of the input power was radiated from the X-point region alone.

In contrast to the boundary conditions used in the marfe models described above, the XPR does not appear in the direct vicinity of a material surface where the plasma temperature can be assumed to be low (<20 eV) due to direct neutral recycling and the presence of impurities from erosion processes. Near the X-point within the confined plasma and with additional external heating, the temperature typically rises above 50 eV. Therefore, a model for the formation of an XPR plasma must start at temperatures above the impurity radiation peak. In addition, the total heating power is no longer linked to the plasma current as in the ohmic discharges addressed by earlier models.

The model presented here for the formation and stability of XPRs is also based on a power balance of the XPR volume. The neutral deuterium density is found to be a key external parameter that triggers XPRs. Furthermore, XPR formation depends on the upstream plasma parameters, safety factor, and flux expansions, as observed experimentally.

By adding a simple particle balance, a condition is found where an XPR evolves into a marfe. Herein, the term marfe will be reserved for the magnetohydrodynamically unstable form of an XPR. The model reproduces the experimentally found scaling of the density threshold for marfes and the differences in marfe occurrence in carbon and metal devices. It also qualitatively recovers a semi-empirical operational diagram found for a real-time marfe avoidance scheme on AUG [24].

The article is organised as follows: section 2 describes the geometry for the model and the solutions of the power balance (section 2.3). In section 3, a condition for XPR formation is derived. Impurity transport introduces more complexity in the model, as discussed in sections 4 and 5 deals with possible future improvements to the model. The model is extended to marfes in section 6 and a marfe occurrence map (figure 9) is introduced. In section 7 the results are discussed and compared with experimental findings. Section 8 concludes the paper.

2. The XPR model

The model for the formation of XPRs is based upon a power balance where the power introduced into the XPR volume by parallel heat conduction from upstream is balanced by losses from atomic processes within the XPR volume. The power balance is established in the simplified geometry introduce in the next section, while the power sources and sinks are specified in section 2.2. Possible solutions of the power balance are discussed in section 2.3.

2.1. Geometry

Figure 1 defines the geometry of the XPR model. The separatrix and the flux surface delimiting the XPR (left figure) form the plasma layer to be analysed using a straight flux tube approximation (right figure). The flux tube is attached to the XPR which is powered by parallel electron heat conduction, $q_\parallel$. The power enters the flux tube upstream from the divergence of ballooned radial heat transport q_r.

The specific magnetic configuration enters the model though the connection length L_c and the flux expansion $f_\mathrm{exp} = \Delta r_\mathrm{X}/\Delta r_\mathrm{u}$, which is the ratio of the radial extend of the XPR and the radial separation of the same flux surfaces at the outer midplane. For the power balance, only the poloidal heat flux component q_θ is relevant that is taken as constant, as losses outside the XPR volume are neglected. q_θ is evaluated upstream from the parallel heat flux $q_\parallel$ and the magnetic pitch angle α_u given by the ratio of the poloidal magnetic field component to the total field strength approximated by the toroidal component, $\sin\alpha_\mathrm{u} = B_\theta/B \approx B_\theta/B_\varphi \approx a/(R_0 q_\mathrm{s})$, using the safety factor for a circular plasma $q_\mathrm{s} = B_\varphi a/(B_\theta R_0)$, with a and R_0 the minor and major plasma radii, respectively. The power conducted into the XPR volume becomes:

$$P_\mathrm{cond,\,e} = 2\pi R_0 \Delta r_\mathrm{u}\ \sin\ \alpha_\mathrm{u}\ q_\parallel \equiv A_\theta q_\parallel, \tag{1}$$

where $A_\theta = 2\pi R_0 \Delta r_\mathrm{u} \sin\alpha_\mathrm{u}$ is a effective poloidal XPR area.

In direction parallel to the magnetic field (z) from the midplane to the X-point, increasing the flux expansion will increase the local Δr and the surface through which the power streams in the poloidal direction. The poloidal heat flux density will decrease, however, together with the local field line pitch angle. This is a direct consequence of the poloidal magnetic

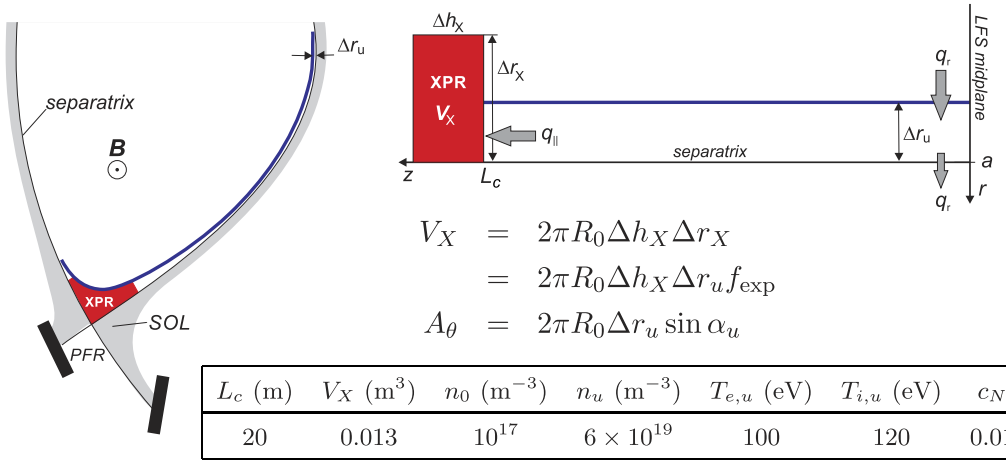

$$V_X = 2\pi R_0 \Delta h_X \Delta r_X = 2\pi R_0 \Delta h_X \Delta r_u f_{\rm exp}$$
$$A_\theta = 2\pi R_0 \Delta r_u \sin\alpha_u$$

L_c (m)	V_X (m^3)	n_0 (m^{-3})	n_u (m^{-3})	$T_{e,u}$ (eV)	$T_{i,u}$ (eV)	c_N
20	0.013	10^{17}	6×10^{19}	100	120	0.01

Figure 1. Definition of the geometry and summary of the parameters used for the XPR model. Left: the XPR volume (*in red*) sandwiched between the separatrix and a flux surface further inside (*in blue*); their radial separation at the outer midplane is $\Delta r_{\rm u}$. Right: the geometry for the treatment of power and particle balances, with a flux tube carrying the parallel heat flux $q_\parallel$ along a connection length $L_{\rm c}$ to the XPR volume. Below the definitions of the XPR volume $V_{\rm X}$, defined by its horizontal and radial extensions $\Delta h_{\rm X}$ and $\Delta r_{\rm X}$, or by the flux expansion $f_{\rm exp} = \Delta r_{\rm X}/\Delta r_{\rm u}$, and the effective poloidal area A_θ, with the upstream field line pitch angle $\alpha_{\rm u}$. The table at the bottom gives the standard parameter set used for quantitative results. The data are for AUG with major and minor radii of $R_0 = 1.65$ m and $a = 0.5$ m, respectively. Further standard parameters used below are $\Delta r_{\rm u} = 1$ mm, $\Delta h_{\rm X} = 5$ cm and $f_{\rm exp} = 25$.

flux conservation within a flux tube. Therefore, the upstream value of $\alpha_{\rm u}$ must be used. It is stressed that the poloidal power flux is substantially lower than the parallel component, which connects thermally the upstream and downstream temperatures along the parallel connection length $L_{\rm c} \sim R_0 q_{\rm s}$.

The XPR volume depends on the choice of the horizontal extend $\Delta h_{\rm X}$ which sets the connection length, defined as the distance along the field line from the outboard mid-plane to the entrance of the XPR. For quantitative estimations, a typical XPR size of $\Delta h_{\rm X} = 5$ cm measured by bolometry is used, which, for a characteristic AUG configuration (cf figure 1), relates to $L_{\rm c} = 20$ m, determined on a flux surface located $\Delta r_{\rm u} = 1$ mm inside the separatrix at the outer midplane. The resulting enclosed XPR volume is $V_{\rm X} \approx 0.013$ m^3.

In the particle and energy balances below, terms related to an influx scaling $\sim A_\theta$ are balanced by volumetric sources and sinks that scale $\sim V_{\rm X}$. This leads to the following useful relation:

$$\frac{A_\theta}{V_{\rm X}} \approx \frac{\sin\alpha_{\rm u}}{f_{\rm exp}\Delta h_{\rm X}} \approx \frac{a}{R_0 f_{\rm exp}\Delta h_{\rm X}}\frac{1}{q_{\rm s}}. \qquad (2)$$

In the following, $\Delta h_{\rm X}$ is kept constant. A change of it requires to adjust $L_{\rm c}$ and $f_{\rm exp}$ in opposite direction. E.g., a smaller $\Delta h_{\rm X}$ will result in a longer connection length and increased flux expansion. Since the geometric quantity (2) relevant for the power and particle balances depends on the product of two inversely related parameters, $f_{\rm exp}\Delta h_{\rm X}$, the exact value chosen for $\Delta h_{\rm X}$ is not very crucial for the scaling results derived below.

2.2. Power sources and sinks

The flux tube connected to the XPR is taken as source free. This approach differs from the SOL model by Lengyel [25] and others [26, 27], where radiation removes energy between the up- and downstream boundaries. Here, the parallel heat flux density $q_\parallel$ in the flux tube of figure 1 is constant. The upstream temperature $T_{\rm u}$ is a given parameter and the downstream temperature $T_{\rm X}$, i.e. the temperature of the XPR, follows from the integration of the parallel heat conduction equation $q_\parallel = \kappa\partial_z T$ from the midplane to the XPR entrance at $z = L_{\rm c}$ (nomenclature as in (16.11) in [28]):

$$T_{\rm X} = \left(T_{\rm u}^{7/2} - \frac{7}{2}\frac{q_\parallel L_{\rm c}}{\hat\kappa}\right)^{2/7} \equiv \left(T_{\rm u}^{7/2} - \frac{q_\parallel}{\hat\kappa_{\rm c}}\right)^{2/7}, \qquad (3)$$

where $\kappa = \hat\kappa T^{5/2}$ is the heat conductivity and $\hat\kappa_{\rm e} = 1820$ W (eV$^{7/2}$ m)$^{-1}$ for the electron fluid. The ion heat conductivity is a factor of 60 lower according to the electron–ion mass ratio in the deuterium plasma analysed here. To simplify the expression,

$$\hat\kappa_{\rm c} = 2\hat\kappa_{\rm e}/(7L_{\rm c}) \sim 1/(R_0 q_{\rm s}) \qquad (4)$$

is introduced. By solving (3) for $q_\parallel$, the power conducted into the XPR volume is estimated from (1) to be

$$P_{\rm cond,e} = A_\theta \hat\kappa_{\rm c}\left(T_{\rm e,u}^{7/2} - T_{\rm X}^{7/2}\right). \qquad (5)$$

For $T_{\rm X} \ll T_{\rm e,u}$ and otherwise the parameters from figure 1, this yields a power source for a developed XPR of $P_{\rm cond,e} \approx 270$ kW.

The method used here to solve the power balance is to link this parallel heat flux (5) to the power dissipated within the XPR rather than the upstream power source, as done in other SOL models. The power balance, apart from the boundary conditions, now only depends on downstream parameters. The main processes that remove power and momentum from the plasma are electron-impact ionisation of neutral deuterium, charge exchange (cx) processes, impurity line radiation and, at temperatures of about 1 eV, recombination [29, 30]. Radial transport is disregarded.

In the presence of impurities in the XPR volume V_X, the electron fluid loses energy by line radiation excitation,

$$P_{rad} = L_z(T_{e,X}) n_X^2 c_N V_X \sim n_X^2 c_N f_{exp}, \quad (6)$$

with the loss function L_z, depicted in figure 2(*a*) for nitrogen in using a coronal approximation, and a nitrogen concentration c_N. This power loss increases quadratically with downstream density n_X. As long as the plasma parameters within the XPR volume are at their upstream values, nitrogen will not add noticeably to plasma cooling. With the values from figure 1, the estimated power loss is only 330 W. Nitrogen's effect will be strongest for $T_{e,X} \approx 5$–20 eV where, in addition, at constant pressure, the XPR density will increase.

Other processes must, thus, be responsible for the initial temperature drop to values where nitrogen radiation can provoke the thermal collapse that forms the XPR. Depending on the neutral deuterium density n_0 or influx Γ_0 electron impact ionization can contribute to the required initial electron cooling. Each ionization removes an ionization energy of $E_{ion} = 13.6$ eV from the electron fluid. In addition, the resulting electron–ion pair is created at the neutral temperature T_0 and both particles must be heated collisionally to the individual background temperatures. The total energy expended by the background plasma for each ionisation process is therefore $E_{ion} + T_{e,X} + T_{i,X} - 2T_0$ and the total loss term related to electron impact ionization becomes

$$P_{ion} = n_X n_0 \langle \sigma v \rangle_{ion} (E_{ion} + T_{e,X} + T_{i,X} - 2T_0) V_X, \quad (7)$$

where the ionization rate $\langle \sigma v \rangle_{ion}$ [32] is plotted in figure 2(*b*). For the standard parameters, about 85 kW are dissipated in a volume with a poloidal cross-section of about 12 cm^2.

The ions lose energy mainly from cx reactions that follow a similar rate coefficient as ionization processes (see figure 2(*b*)). The power dissipated by cx reactions between deuterium ions and deuterium neutrals is

$$P_{cx} = n_X n_0 \langle \sigma v \rangle_{cx} (T_{i,X} - T_0) V_X. \quad (8)$$

This energy is removed from the ions, where a hot particle is substituted by one at the neutral temperature T_0 (typically 3 eV). For the standard parameters the power loss is about 60 kW.

The two plasma components are coupled through collisional energy transfer from the hotter to the colder species. The electron–ion energy transfer rate is given by (equations (8.62) and (8.64) in [28])

$$Q_{ei} = \left(\frac{e^2}{4\pi\epsilon_0}\right)^2 \frac{4\sqrt{2\pi m_e}\ \ln\Lambda}{m_i} n_X^2 \left(\frac{T_{i,X} - T_{e,X}}{T_{e,X}^{3/2}}\right).$$

In a situation where the XPR electron temperature is $T_{e,X} = 10$ eV and the ion fluid is still at the upstream value of $T_{i,X} = 120$ eV, the power transfer from the ions to the electrons, $P_{ei} = Q_{ei} V_X$, for the standard parameters is of the order of 3 MW. This far exceeds any contributions from individual source and sinks and consequently, inside the XPR electron and ion fluids may be treated as energetically closely coupled. Furthermore, since the thermal conductivity of ions is 60 times lower than that of electrons, the energy exchange will cool the ions to the electron temperature, $T_X \equiv T_{i,X} = T_{e,X}$, and the ion channel power loss must also be compensated by electron heat conduction.

A condition for the downstream density can be derived from the pressure balance. Without particle sources or sinks outside the XPR, integrating the 1D ion equation of motion along the field line yields constant total kinetic pressure $p = p_e + p_i$ on flux surfaces:

$$\partial_z p_i + en\partial_z\phi = \partial_z(p_i + p_e) = 0 \Rightarrow n(T_e + T_i) = \text{const.} \quad (9)$$

The electrostatic force $-\partial_z\phi$ was replaced by the electron pressure using the Boltzmann relation. For the downstream density as function of the upstream and downstream electron and ion temperatures and a given upstream density n_u this yields:

$$n_X = \frac{T_{e,u} + T_{i,u}}{T_{e,X} + T_{i,X}} n_u. \quad (10)$$

To reach high densities in the cold XPR volume, as it will become important below, both electron and ion fluids need to be at a low temperature. The ion–electron energetic coupling helps, according to (10), to increase the downstream density and, in turn, to increase the loss terms.

Experiments indicate [33, 34] a kinetic pressure drop on open field lines between the outer midplane and the divertor target region, when the temperature in the divertor falls to values $\leqslant 10$ eV. The pressure loss was attributed to ion–neutral friction [35]. In contrast to open field lines, where there is a natural particle sink at the divertor target and thus a parallel flow, on closed field lines, parallel flows (beyond the equilibrium flow) are expected only when recombination, e.g., within the XPR volume, occurs at $T_X \leqslant 3$ eV. This will only play a role in a detailed treatment of the power balance for the investigation of marfe occurrence in section 6. At high-temperature (>20 eV), the constancy of the pressure between the X-point region and upstream is also confirmed by the Thomson scattering measurements shown in figure 10. It should also be pointed out that the neutral densities producing a pressure drop in the SOL [33–35] are typically two orders of magnitude higher than the values relevant for XPR occurrence.

2.3. Power balance

A consistent power balance solution for the XPR plasma requires that power losses in the electron and ion channels (equations (6)–(8)), calculated at the downstream parameters n_X and $T_X = T_{i,X} = T_{e,X}$, match the heat flow into the XPR volume (5). Figure 3(*a*) shows the individual power sources and sinks of the XPR volume as a function of the downstream temperature. Upstream density and temperatures are parameters and the downstream density follows from (10).

The description of the power balance in figure 3(*a*) begins at $T_X = T_{e,u} = 100$ eV, where heat conduction (5) vanishes but the ionisation and charge-exchange losses from the XPR volume remain finite. The net power loss causes a decrease in T_X until the red dashed-dotted line showing the heat conduction

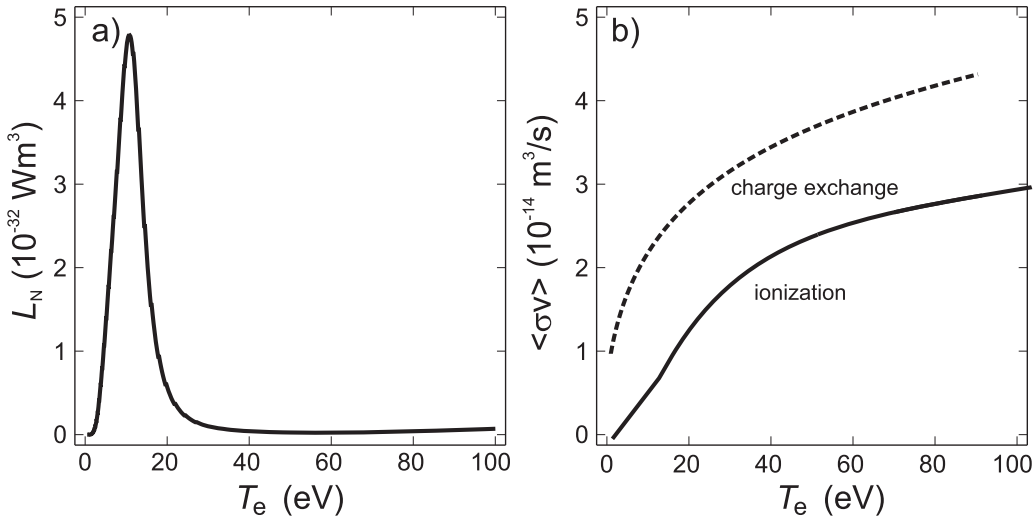

Figure 2. Left: radiation curve for nitrogen in corona equilibrium from [31] and (right) rate coefficient for electron-impact ionization and cx processes for hydrogen from [31, 32], respectively.

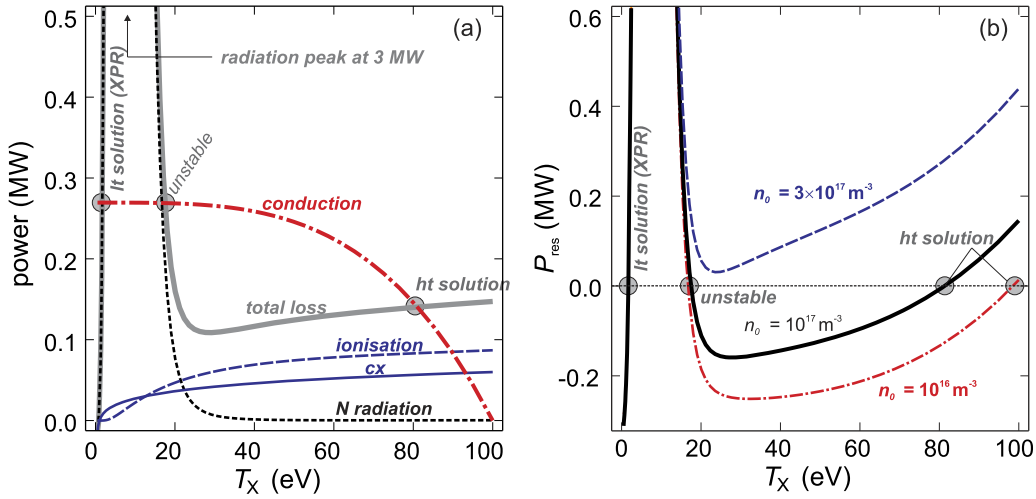

Figure 3. (*a*) Sink and source terms of the power balance for the XPR as function of downstream temperature for standard parameters from figure 1 and $c_N = 1\,\%$. Nitrogen radiation losses dominate at low temperatures; the maximum of the radiation peak is outside the scale of the figure at about 3 MW. The *grey line* represents the sum of the three loss terms and the *red dashed–dotted line* the power carried by conduction. (*b*) Power balance residuum (11) for three values of the neutral density. The *black line* represents the case from the left figure. Stable low-temperature (lt) and high-temperature (ht) solutions are indicated.

crosses the thick grey line tracing the sum of all losses. A high-temperature (ht) solution is reached at $T_X \approx 80$ eV. This solution is stable since a further reduction in T_X leads to an increase in power conducted into the volume with near constant losses, and T_X is pushed back to its stable value.

Further solutions of the power balance occur when nitrogen starts to radiate more strongly as T_X approaches 10–20 eV. Here, nitrogen radiation dominates the losses. The intersection of the heat conduction line with the right flank of the total loss function (grey) is, however, an unstable solution: further lowering of the temperature increases radiation losses, that, in turn, further cool the plasma. This sequence describes the thermal collapse of the plasma related to the impurity radiation peak. Consequently, the temperature decreases until the stable low-temperature (lt) solution is reached in the few-eV range, the XPR.

Once reached, the low-temperature solution can even be maintained when the neutral density is suppressed. The plasma solution is virtually trapped at the low temperature. The XPR would vanish only if the nitrogen concentration (here 1 %) drops significantly reducing the radiation peak. For the simulated parameters, this would happen at $c_N < 0.1\,\%$.

The plasma access to the low-temperature solution depends on several parameters and is addressed in the next section. To illustrate the physics behind this question, figure 3(*b*) shows the power balances, i.e. the sum of all losses minus the conducted heat,

$$P_{res} = P_{rad} + P_{ion} + P_{cx} - P_{cond,e}, \qquad (11)$$

for three values of the neutral deuterium density. At negative values of the power balance residuum P_{res} (the X-point

plasmas receives more heat than it loses), the X-point temperature will increase, whereas for a positive residuum the losses will reduce T_X. The form of the curves is generic and was also discussed in a work on a *phase* model for the plasma edge of limiter tokamak plasmas [36].

The formation of an XPR by changing the boundary conditions, here as an example n_0 or the gas fuelling, is presented starting from the standard parameter set (figure 1), with $T_X \approx T_u$ and $n_X \approx n_u$. In the coronal limit at the high temperature, nitrogen is essentially fully ionized and the radiation losses can be neglected. Up to neutral deuterium densities of 10^{16} m^{-3} (red dotted–dashed line in figure 3(*b*)) ionization and charge-exchange losses are also small and $T_X \approx T_u$ is preserved. As the neutral density increases, the losses increase causing a continuous reduction of the X-point temperature. At a neutral deuterium density of about 10^{17} m^{-3} the power balance corresponds to that of figure 3(*a*) and to the black solid line in figure 3(*b*), with T_X given by the stable high-temperature solution. Since the temperature cannot decrease further, a XPR does not develop. The situation changes when the neutral deuterium density increases further to about 3×10^{17} m^{-3}, as represented by the blue dashed curve in figure 3(*b*). Here, ionisation and charge-exchange losses dominate over the heat conduction. As a consequence, the temperature will continue to fall beyond the nitrogen radiation peak until the low-temperature or XPR solution is reached.

From the above discussion it is concluded, that losses related to neutral deuterium can play an important role for the initial reduction of the X-point temperature and the XPR development. In the coronal limit, nitrogen only enters the process when the temperature has decreased in the range of 20 eV. Only then can an XPR develop with a temperature in the range of 1 eV, where also recombination reactions will contribute. Non-coronal effects and the influence of transport processes on conclusions drawn in this and the following section will be discussed in section 4.

3. XPR access condition

XPR access has been shown to depend on the loss of the high-temperature solution, which in turn is mainly determined by power losses related to neutral deuterium. Nitrogen radiation will therefore be neglected in the formulation of an XPR access condition. The following simplified forms for the three dominant contributions to the power balance are used.

The maximum possible heat conducted into the XPR volume is $P_{cond} \approx A_\theta \hat{\kappa}_c T_u^{7/2}$ (cf (5)). Ionization and charge-exchange losses are approximated by setting the plasma parameters to their upstream values. From (7) $P_{ion} \approx 2\langle\sigma v\rangle_{ion} n_u n_0 T_u V_X$, where E_{ion} and $2T_0$ were neglected against $2T_u \approx T_{e,u} + T_{i,u}$, and from (8) $P_{cx} \approx \langle\sigma v\rangle_{cx} n_u n_0 T_u V_X$. An XPR emerges when losses exceed the conducted power, $P_{ion} + P_{cx} > P_{cond}$. From this follows the *XPR access condition*

$$X_A \equiv \left(2\langle\sigma v\rangle_{ion} + \langle\sigma v\rangle_{cx}\right) \frac{V_X}{A_\theta \hat{\kappa}_c} \frac{n_u n_0}{T_u^{5/2}} > 1. \qquad (12)$$

For figure 3(*b*), an XPR develops when $n_0 \approx 3 \times 10^{17}$ m^{-3}. For the same parameters, $\langle\sigma v\rangle_{cx} = 3 \times 10^{-14}$ m^3 s^{-1} and $\langle\sigma v\rangle_{ion} = 4 \times 10^{-14}$ m^3 s^{-1} (cf figure 2(*b*)), the *XPR parameter* becomes $X_A \approx 1.4 > 1$, which shows that criterion (12) is consistent with the full power balance shown in figure 3.

While the absolute value of X_A may only be a rough estimate, its parameter dependencies should be more robust. Inserting the geometric relation (2) and the leading parameters of $\hat{\kappa}_c$ (4) yields a scaling expression for the XPR parameter that takes the form

$$X_A \sim \frac{R_0^2 q_s^2 f_{exp}}{a} \frac{n_u n_0}{T_u^{5/2}}. \qquad (13)$$

An XPR forms at high X_A values, i.e. at high upstream density, low upstream temperature and high neutral particle density near the X-point. These conditions are often only met close to the density limit. XPR access is furthermore favored in magnetic configurations with a high safety factor and aspect ratio, R_0/a, in regions of high flux expansion, as present above the X-point.

Using the SOL two-point model [30], the XPR parameter scaling (13) can be reformulated in terms of engineering variables. Here, the upstream temperature is estimated from the net power flux crossing the separatrix according to ((16.34) from [28])

$$T_u = \left(\frac{1}{\chi_r n_u \hat{\kappa}}\right)^{2/9} \left(\frac{7 L_{SOL} P_{sep}}{2S}\right)^{4/9}. \qquad (14)$$

Here, χ_r is the radial heat diffusivity, S the separatrix surface area, and L_{SOL} the SOL connection length measured from the midplane to the divertor target $L_{SOL}/S \sim q_s/a$. Substituting (14) into (13) provides a leading engineering parameter dependency of the XPR parameter:

$$X_A \sim R_0^2 q_s^{8/9} f_{exp} n_0 n_u^{14/9} P_{sep}^{-10/9}. \qquad (15)$$

Compared with (13), the use of power, rather than temperature, leads to a weaker, still near linear, dependence on q_s. The density dependence remains strong whereas high heating power hampers XPR formation. For given discharge parameters, the neutral density can be used as the external trigger to initiate an XPR by increasing X_A. Since P_{sep} is the net power crossing the separatrix, increased radiative losses in the edge plasma, e.g. caused by argon seeding [37], can also cause an XPR to develop. As discussed in section 7.1, our derived parameter dependencies for XPR formation agree with experimental observations.

Finally, the parameter space in which an XPR can develop is examined through the full power balance that includes nitrogen radiation losses. Figure 4 summarizes the solutions of the power balance for systematic scans of the upstream and the neutral density in the ranges 4–8 $\times 10^{19}$ m^{-3} and 0.1–7 $\times 10^{17}$ m^{-3}, respectively, with the other parameters kept constant. Figure 4(*a*) shows a contour plot of the high-temperature solutions. Where such a solution exists, the XPR cannot develop. An increase in n_u or n_0 can lead, however, to a reduction in the X-point temperature to below 30 eV. An XPR will only develop in the top right sector where the density is highest.

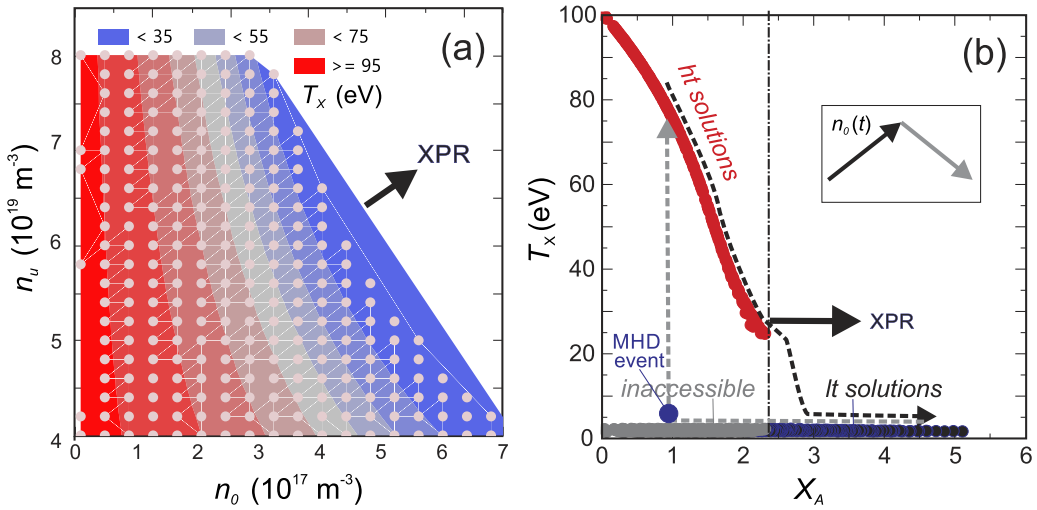

Figure 4. Solutions for the power balance when n_u and n_0 are independently varied in the ranges 4–8 $\times 10^{19}$ m^{-3} and 0.1–7 $\times$ 10^{17} m^{-3}, respectively. Otherwise standard parameters are used. (*a*) Stable high-temperature solutions for T_X (color coded) as a function of the value pairs upstream and neutral density indicated by the dots. (*b*) Ordering of all solutions with the XPR parameter (12). For $X_A \leqq 2.3$, the high-temperature solutions (*red dots*) shield the low-temperature solutions (*grey dots*). The latter are accessible (*black dots*) for $X_A \geqq 2.3$ only. The dashed line indicates a possible dynamic evolution of T_X in response to the neutral density being ramped up (*black*) and down (*grey*) as shown in the *inset*.

Figure 4(*b*) illustrates, how the XPR parameter (12) structures the solutions found in the n_u and n_0 scans. Only where X_A exceeds a critical value of about 2.3, can the low-temperature or XPR solution be obtained. This value differs from 1, as, now, the full power balance was solved. Grey markers indicate inaccessible low-temperature solutions, that are in the 'shadow' of a stable high temperature solution. These shielded solutions could, however, be obtained in a dynamic situation, where, e. g. the neutral density, is ramped up until an XPR forms and then ramped down to X_A values to below the criticality. This possible trajectory is traced by the dashed black and grey lines in figure 4(*b*). Here, the XPR solution would remain trapped at temperatures below the nitrogen radiation peak (see figure 3). Where the nitrogen impurities are periodically flushed out by MHD activity such as ELMs, this process may generate an oscillatory behavior with a hysteresis as indicated. Similarly, oscillations between the low and high-teperature solutions can be triggered by an MHD instability of the XPR itself as proposed by in Ryutov *et al* [38]. This is a special example of a bifurcation causing oscillations which are common in divertor plasmas as pointed out and described in [39].

4. Influence of transport on the model solutions

In this section, the validity of two assumptions which were used to set up the power balance are addressed, (i) a constant neutral density to calculate ionization and charge-exchange losses and (ii) the coronal power loss function used to estimate impurity radiation losses. In a real plasma, both quantities will depend on transport.

(i) Neutral deuterium crossing the separatrix is rapidly ionized and the neutral density decays quickly with distance from separatrix to core. Rather than a constant neutral density, the net flux of neutral deuterium Γ_0 into the considered volume could be used. These quantities are related through a neutral particle balance of the form

$$\Gamma_0 = n_X n_0 \langle \sigma v \rangle_{ion} V_X, \tag{16}$$

where the ionization rate represents an average value estimated from integrating over the volume V_X. For standard parameters ($n_0 = 1 \times 10^{17}$ m^{-3}, and $T_X = T_u$) follows $\Gamma_0 \approx 5 \times 10^{20}$ s^{-1}. This is about 10 % of the total particle fuelling rate needed on AUG to maintain a plasma density of 10^{20} m^{-3} when the particle confinement time is estimated to be 100 ms. These values appear reasonable as the contribution of the X-point region to fuelling. Substituting n_0 by Γ_0 does not change the essence of the above results.

(ii) It is well known [40] that impurity radiation losses are enhanced above the coronal level when charge-exchange with neutral hydrogen repopulates radiating electron states of highly ionized ions. Non-coronal effects were included in 1D SOL transport models for detachment studies [26, 27, 41]. Recently, it was shown that non-coronal processes significantly alter the power balance of impurity seeded fusion plasmas [42]. The influence of transport effects on the nitrogen radiation losses from the XPR volume was simulated for our situation. Two effects are relevant: enhanced radiation when impurities are considered to enter the volume as neutral particles, and additional radiation resulting from repopulation of ionized states by charge-exchange.

Nitrogen transport was simulated in the XPR geometry of figure 1, where neutral nitrogen enters the X-point volume through the private flux region (PFR). During the dwell time τ_N in the X-point volume, the nitrogen is ionized gradually and radiates until again exiting the volume. The dwell time is estimated from the thermal parallel velocity of nitrogen ions in the range 0.05–0.2 ms, for T_X in the 100 to 10 eV range. The density, n_X, was obtained from the constant pressure constraint

(10) with $n_u = 3 \times 10^{19}$ m^{-3} and $T_{e,u} = T_{i,u} = 100$ eV. Up to a neutral deuterium density of $n_0 = 10^{17}$ m^{-3}, simulations indicate that charge-exchange effects have a weak influence on the power radiated per nitrogen atom during its dwell time in the X-point volume.

Figure 5 illustrates the changes in the power balance (11) when realistic radiation losses are used. In the temperature range of 20–50 eV, in figure 5(*a*) an radiation loss enhancement by transport is visible, where inclusion of charge-exchange increases the losses only marginally. This leads to a wider radiation peak than that in coronal approximation.

Similar to figure 3(*b*), figure 5(*b*) presents the power balance residuum for three nitrogen concentrations. With respect to figure 5(*a*), the upstream density was increased to $n_u = 4 \times 10^{19}$ m^{-3} and the neutral density reduced to $n_0 = 10^{16}$ m^{-3}. The figure thus illustrates how an XPR can be created by impurity seeding with moderate deuterium fuelling and density. Here, the unstable power balance solution shifts to higher temperatures but a stable high-temperature solution remains that prevents a radiative collapse. Only at high impurity concentrations of $c_N > 3\,\%$ does the high temperature solution disappear so an XPR can form, as for the high neutral densities in figure 3(*b*).

Transport effects have little influence on the radiation losses for temperatures in the 1 eV range. A discussion of the exact value of the low-temperature solution will be done in section 6.

In conclusion, impurity transport influences the solutions obtained on the basis of the coronal approximation, but mainly only quantitatively. However, there is a synergy between power losses introduced by neutral deuterium and impurities. A higher neutral deuterium density, or a higher nitrogen concentration, will reduce the X-point temperature and may lead to a loss of the high-temperature solution with the consequence of XPR formation. An XPR can occur in a density ramp at low impurity density but also with a moderate gas feed when impurities are strongly puffed.

5. Radiating mantel of the XPR

Before discussing the stability of the XPR and the emergence of marfes in the next section, some shortcomings of the model in the case of the low-temperature (or XPR) solution will be discussed here.

The fact that the effect of neutral deuterium and impurities is limited to the XPR volume makes the model 0D. Radiation losses outside the XPR volume enter only implicitly through the upstream temperature, which is used as a parameter: strong radiation losses in the plasma edge will reduce T_u and, thus, the power conducted into the XPR volume.

This approximation does not critically affect the XPR access condition. At the low-temperature solution, however, T_X is too low to provoke strong radiation and the plasma becomes transparent to neutral deuterium and impurity atoms. As also discussed in [14], the neutral particles can diffuse across the actual XPR boundary and interact with the hotter upstream plasma to form radiation and ionisation fronts as known from detached divertor plasmas. This results in a radiating mantel around the low-temperature plasma which can be regarded as a cold XPR core. Indeed, recent SOLPS-ITER simulations of a nitrogen-seeded AUG plasma [43] support such a picture: the simulation result in figure 6 shows a 2D radiation pattern of an XPR resembling that of a black hole, with a bright radiating ring around a fainter shining core. Similarly, the experimentally observed radiation may arise at the border of the cold plasma which is identified in the model with the XPR. The XPR access condition is not affected by these considerations since the related power losses are only relevant in the presence of the low-temperaure solution. It will, however, influence the XPR stability, which is described in section 6.2.

An improved model that includes an integral over the upstream power losses would require an extension to 1D, as it is typical for divertor detachment studies [25–27, 40]. For such an extension to be realistic, the spatially varying impurity concentration would need to be known. The additional losses reduce both the power conducted into the XPR volume and the temperature of the developed XPR.

Furthermore, an extended model must account for the particle source that arises from electron impact ionization outside the XPR region. The effect of ionisation on the power balance approximately cancels since convective energy transport is neglected as XPR energy source. On the other hand, a particle balance must be included in the model, where ionisation provides the particle source for a particle flux into the XPR volume. The latter plays a key role in the onset of marfes, as treated below. In the following, the particle source of the developed XPR will be given by the plasma influx at the ion sound velocity. Consequently, the kinetic pressure cannot be considered as constant anymore, and (10) must be replaced by

$$n_X = \frac{T_u}{2T_X} n_u, \tag{17}$$

which includes the contribution of the static pressure (see e.g. equation (5.4) in [30]). This relation will be used in the particle balance introduced in section 6.1, where the occurrence of marfes is discussed.

6. XPR stability and marfe formation

This section is devoted to the low-temperature (i.e. XPR) solution of the power balance. The discussion includes the dependence of the XPR temperature on impurity species and, by including a simple particle balance, a stability criterion that describes the process of an XPR developing into a marfe.

6.1. Particle balance for the XPR volume

For typical XPR temperatures of 1 eV, electron–ion recombination processes become an increasingly important particle sink. The corresponding particle loss rate within the XPR volume is

$$\Gamma_{rec} = n_X^2 \langle \sigma v \rangle_{rec} V_X, \tag{18}$$

where the recombination rate coefficient $\langle \sigma v \rangle_{rec}$ can be taken from [31]. At temperatures well below the ionization energy of deuterium, ionization can be neglected as particle source. In order to maintain a stationary plasma, recombination losses must thus be balanced by radial and parallel particle transport.

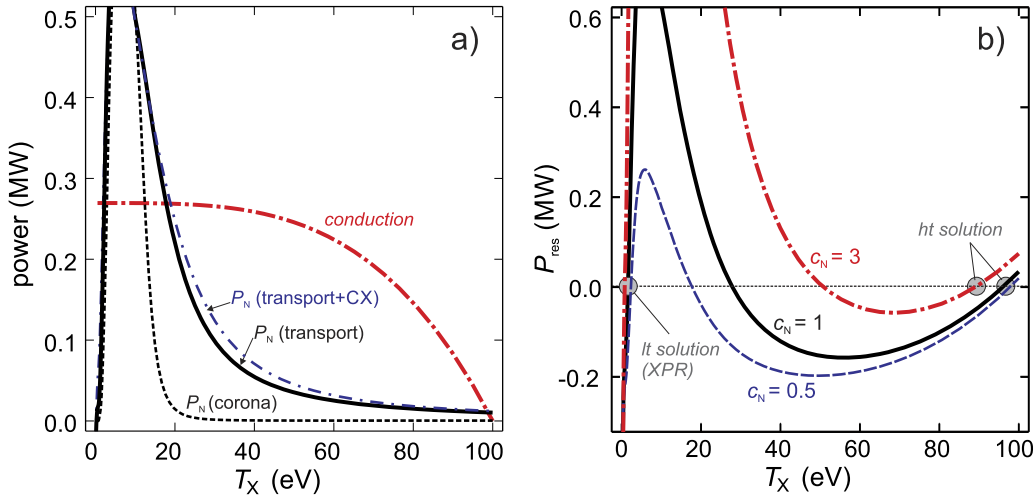

Figure 5. Similar as figure 3 but with the nitrogen loss function including transport effects instead of the corona model. (*a*) Radiation losses from transport calculations (see text) without (*solid line*) and with charge-exchange effects (*blue dashed–dotted line*) for $T_{e,u} = T_{i,u} = 100$ eV; $n_0 = 10^{17}$ m^{-3}, $n_u = 3 \times 10^{19}$ m^{-3} and $c_N = 1$ %. The curve in corona approximation (*dashed line*) and the heat conduction power are plotted for reference. (*b*) Power balance residuum (11) for $n_0 = 10^{16}$ m^{-3}, $n_u = 4 \times 10^{19}$ m^{-3} and three nitrogen concentrations including cx and transport effects.

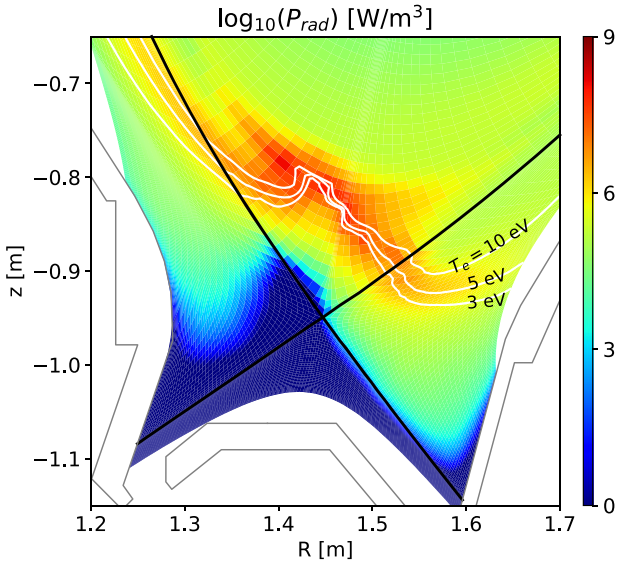

Figure 6. Radiation power distribution around the X-point from a SOLPS-ITER simulation including plasma drifts of the nitrogen seeded AUG H-mode discharge #36655. White lines indicate contours for three the electron temperatures. A strongly radiating mantle wraps around the cold XPR core. The figure serves as an illustration, details of the simulations will be published elsewhere [43].

Here, particle transport is treated in the same way as heat conduction in the power balance. It is assumed that only parallel transport can provide a particle source for the XPR. Since parallel convection in response to a pressure imbalance occurs at the ion sound speed, $c_s = (2T_X/m_i)^{1/2}$, the maximum poloidal particle flux into the XPR volume can be estimated by (cf (1))

$$\Gamma_{in} = 2\pi R_0 \Delta r_u \sin \alpha_u c_s n_X = A_\theta c_s n_X. \qquad (19)$$

It is well established that a supersonic flow may exist at the transition to the cold plasma volume [44–47]. This could be accounted for by an additional factor, but would not have a strong impact on the results that depend more strongly on scaling behavior.

Once the particle loss by recombination exceeds the maximum possible particle influx, the pressure in the XPR volume will decrease and a *pressure hole* develops. In the same way as a pellet ablation cloud [48], or a plasma blob in the SOL [49], are advected in the direction of lower magnetic field strength by the interchange drive, a pressure hole will be advected in the high-field side direction. The physical mechanism can be understood by considering the diamagnetic current along the pressure contours which, because of the pressure drop, enclose the XPR. Because of the inhomogeneous magnetic field, the current is not divergent-free, so that electric charges and fields are created which advect the plasma in the direction where the field is stronger. This instability is proposed as the driving mechanism which transforms a stable XPR into a non-stationary marfe. It could be that the XPR must first grow to a certain size before this mechanism can take effect.

As criterion for marfe formation $\Gamma_{rec} > \Gamma_{in}$ will be used. Substituting in (18) and (19) n_X with (17) and using $T_u = T_{e,u} = T_{i,u}$ this relation becomes:

$$\frac{\langle \sigma v \rangle_{rec}(T_X)}{T_X^{3/2}} > \sqrt{\frac{2}{m_i}} \frac{A_\theta}{V_X} \frac{2}{n_u T_u}. \qquad (20)$$

Figure 7 compares the two contributions to the particle balance for the standard parameters. The exponentially increasing recombination rate at low temperature (left side) dominates. At the given parameters and $T_M = T_X \approx 1.2$ eV, recombination and convection contributions cancel. For $T_X \leqslant T_M$ recombination exceeds convection. Because the right side of (20) is constant, the losses cannot be balanced: a stationary situation

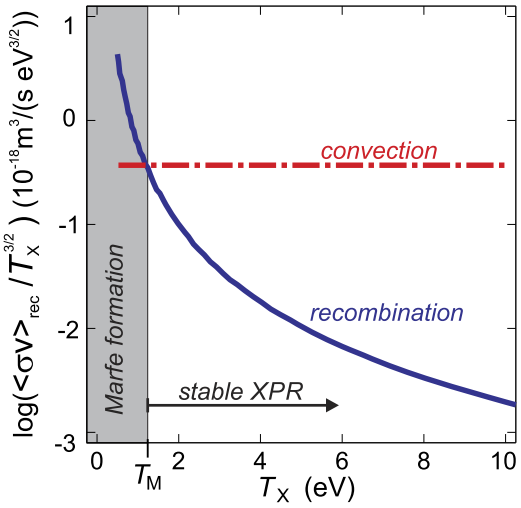

Figure 7. The two terms of (20) as function of the XPR temperature for the standard parameters. For $T_X < T_M$ *recombination* losses (left side of (20)) exceed the *convection* source (right side), and a marfe can form. Note the logarithmic scale.

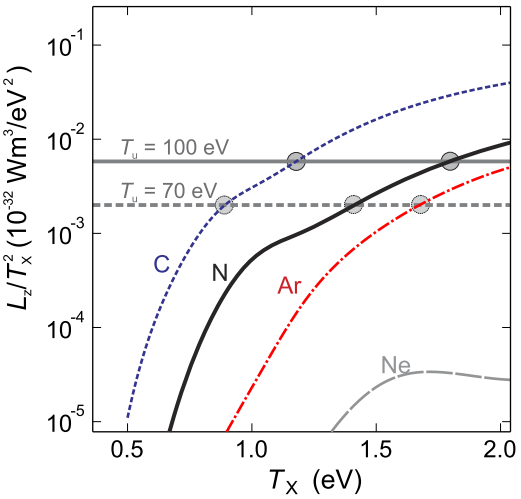

Figure 8. Radiation loss curves for the impurities carbon, nitrogen, neon and argon divided by T_X^2 according to (22). Horizontal lines represent the right side of (22) for the standard parameters (*full line*) and at reduced temperature, $T_u = 70$ eV and $n_u = 8 \times 10^{19}$ m^{-3} (*dashed line*). Here an increased value of $c_{imp} = 4\,\%$ was used. *Circles* indicate the low-temperature solutions of the power balance.

cannot be reached and a marfe can form. For $T_X > T_M$ particle convection is strong enough to maintain a constant pressure on the magnetic field lines and the XPR remains stable.

6.2. Marfe formation criterion

The XPR temperature in (20) is set by the power balance (cf section 2.3) which, at these low temperatures, is practically independent of ionization and charge-exchange losses. Therefore T_X can be estimated from a simplified power balance, resulting from the impurity radiation losses (6) and the heat conduction source (5):

$$L_z(T_X) n_X^2 c_{imp} V_X = A_\theta \hat{\kappa}_c T_u^{7/2}, \tag{21}$$

where the impurity concentration c_{imp} refers to the considered species and $T_X \ll T_u$ was used. Again substituting n_X with (10) leads to an equation, that can be solved numerically to obtain the XPR temperature:

$$\frac{L_z(T_X)}{T_X^2} = \frac{T_u^{3/2}}{n_u^2} \frac{\hat{\kappa}_c A_\theta}{V_X} \frac{4}{c_{imp}}. \tag{22}$$

T_X depends now on the impurity species specified through the loss function L_z. Figure 8 plots the rapid decrease of the left side of (22) with temperature, whereas the right side depends only upon upstream parameters, geometry and impurity concentration. The horizontal solid grey line represents this value calculated for our standard parameters, while, for the dashed line, the upstream density was increased and the temperature decreased. The crossing points indicate the low-temperature power balance solutions for T_X. The corresponding temperatures are clearly in the range where marfes can develop. The lowest temperatures are found with carbon, then nitrogen and argon, while neon's equilibrium temperature is well above 2 eV and will not provoke a marfe.

The convected heat can be neglected in (21) in good approximation. The ratio of convected (19) to the conducted (5) energy

$$\frac{2 T_X \Gamma_{in}}{P_{cond,e}} \approx \frac{c_s n_u}{\hat{\kappa}_c T_u^{5/2}}$$

corresponds to only a few percent.

6.3. Parameter dependence of marfe occurrence

Figure 9 shows a marfe occurrence map in the upstream density-temperature space. For each parameter pair, the XPR temperature was calculated numerically from the simplified power balance (22) and this value was inserted into the particle balance (20) to see whether the solution is stable or whether a marfe can occur. The horizontal lines in the figure separate the parameter space where an XPR will be stable (below the lines) from that where it may transform into a marfe (above).

This exercise was performed for the four impurities addressed in figure 8. With the given boundary conditions, an XPR with carbon impurities will almost always develop into a marfe while with nitrogen, and more with argon, stable XPR solutions are found up to upstream densities of 7×10^{19} m^{-3} and 1×10^{20} m^{-3}, respectively. For neon, with these parameters, the XPR is always stable since the temperature remains above 3.5 eV where the recombination rate is sufficiently low. Neon would require much higher concentrations to form a marfe at experimentally accessible upstream densities.

It is surprising that the boundary between stable XPRs and marfes depends only weakly on the upstream temperature. It is the density that is mostly determinant in this plot, when impurity concentration and geometry are kept fixed. This observation can be understood by inspecting (20) and (22) simultaneously. The second sets the XPR temperature and the

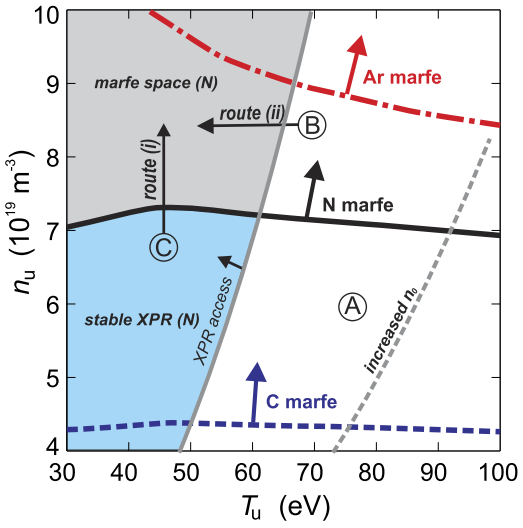

Figure 9. Boundaries between ranges of stable XPR solutions (*below*) and marfe solutions (*above the horizontal lines*) for the impurities carbon, nitrogen and argon. Neon produces stable XPRs everywhere. *Grey vertical lines* mark the XPR access according to (12) for the standard parameters and the *dashed grey line* for the higher neutral density of 3×10^{17} m^{-3}. For nitrogen seeding a marfe can develop in the grey area. For Ⓐ– Ⓒ and the *routes* it is referred to the text.

first the stability at that temperature. Unstable solutions are favored when the right sides of both relations are small. To obtain a scaling expression for marfe formation, the inverse of the product of the two terms is taken. Together with (2) and (4), the resulting *marfe occurrence parameter* has the form

$$M_A = \frac{R_0^3}{a^2}\sqrt{\frac{m_i}{T_u}} n_u^3 q_s^3 f_{exp}^2 c_{imp}, \tag{23}$$

where a high value of M_A promotes the occurrence of a marfe. The parameter dependencies represent different physical processes: marfes are promoted by low power and particle inflows, i.e. small pitch angles ($\sin^2\alpha^2 = R_0^2 q_s^2/a^2$) and long connection lengths ($L_c = R_0 q_s$). Furthermore, a big XPR volume ($V_X \sim f_{exp}$) promotes marfes by increasing the losses which also grow with n^2. The dependence on ion mass is due to the sound velocity defining the particle source, which has a stabilizing effect at high values.

This criterion reflects the leading roles of the upstream density and the safety factor, as found in experiment. A critical upstream density n_M, where a marfe forms, will be lower for higher values of the safety factor and the impurity concentration. The weak temperature dependence is also recovered. From (14) it corresponds to a even weaker power dependence than reported from experiment [24]. Assuming that the transition to a marfe occurs for a threshold value of M_A, a scaling of the critical density for marfe formation can be derived from (23). At fixed geometry, the leading parameters of the *critical density for marfe occurrence* are:

$$n_M^{(i)} \sim \frac{1}{q_s c_{imp}^{1/3}}. \tag{24}$$

A common experimental finding for carbon devices is that the density is the main parameter controlling marfe formation with a scaling of the form $n_m \sim 1/(q_s c_{imp}^{0.5})$ [4] (and references therein) that is in good agreement with (24). A recent study of the H-mode density limit in AUG with a tungsten wall found also an inverse, though somewhat weaker, dependence of the critical density on the safety factor, i.e. $n_M \sim I_p^{0.27} q_s^{-0.32} \sim q_s^{-0.6}$ [24, 50].

6.4. Routes to a marfe

Finally the results related to marfe formation from the previous section and those related to XPR formation from section 2.3 are combined. In the discussion of marfe formation the very presence of a low-temperature plasma solution for given parameters was ignored. Access to a low-temperature plasma solution according to criterion (12) is a prerequisite for the formation of a marfe: an XPR must first be able to form before it may become unstable. To link the conditions for the two processes, the XPR access condition (12) is rewritten as a condition on the upstream density,

$$n_u > \frac{2A_\theta \hat{\kappa}_c}{V_X\left(2\langle\sigma v\rangle_{ion} + \langle\sigma v\rangle_{cx}\right)} \frac{T_u^{5/2}}{n_0}, \tag{25}$$

that is represented by two vertical grey lines in figure 9. The solid grey line is evaluated for our standard parameters and the dashed one for the higher neutral density $n_0 = 3 \times 10^{17}$ m^{-3}, where, in figure 3, the low-temperatre solution became accessible. In the domain left of these lines, the XPR solution can be reached since it is not shielded by the high-temperature solution. The impurity species does not affect these lines. This may change, when impurity losses are enhanced by transport effects as discussed in section 4. At the higher neutral deuterium density (dashed line), the marfe territory is pushed substantially to higher upstream temperatures. Here, it is the neutrals that open access to the low-temperature plasma solution. Both boundaries, for XPR and for marfe formation, can be displaced according to the dependencies described in (25) and (24), respectively.

The right side of (25) represents an alternative expression for the critical density n_M of marfe occurrence. Substituting the upstream temperature by the power crossing the separatrix using (14) and setting $n_u = n_M$ results in an expression that is solved to obtain the engineering parameter dependence of the *alternative critical marfe density*:

$$n_M^{(ii)} \sim \frac{P_{sep}^{5/7}}{n_0^{9/14} q_s^{4/9}}. \tag{26}$$

This expression follows also directly from (15). It differs from (24) by a dependence on power crossing the separatrix and a weaker q_s strength. Under the used coronal approximation, it is independent of the impurity concentration but scales inversely with the neutral deuterium density.

Whether expression (24) or (26) is the relevant scaling for the critical density of marfe occurrence depends on the discharge scenario as illustrated in figure 9: in a strongly heated discharge with an upstream temperature above 70 eV, as indicated by Ⓐ, a density increase will evolve the edge plasma parameters from Ⓐ to Ⓑ. Although the parameters at Ⓑ

fulfill the criterion for a marfe in nitrogen, no marfe will occur as the XPR criterion (25) is still violated. This discharge edge remains stationary at the high-temperature solution Ⓑ. For this plasma, marfe occurrence now underlies the criterion for XPR access, with the density scaling (25) or (26). Here, a gas puff, increasing the neutral density, or a loss of heating power, reducing the temperature, may produce a marfe along route (ii).

A plasma at lower heating power, with parameters corresponding to position © in figure 9, will, however, have a stable XPR and any transition to the unstable state along route (i) will be governed by the marfe criterion (23), where the density plays the leading role.

This discussion illustrates that, depending on the experimental approach, different parameter dependencies can be displayed for marfes occurrence. In a tungsten device, depending on heating power, both sketched routes to a marfe can occur, while in an ohmically, or in a low power heated carbon device, where early experiments were performed, an XPR would already develop at low densities and should be expected to be less stable than in a tungsten device with strong auxiliary heating. Here, a transition to a marfe along route (i) can be expected following criterion (23) with the critical density scaling (24). In both cases, the upstream density is a key parameter for the occurrence of marfes. Along route (i), i.e. at low heating power, the critical density (24) does not depend strongly upon power but on impurity density, whereas for clean, high power discharges, the critical density (26) increases with power and decreases with neutral deuterium density. Along both routes, the critical density will be lower for higher values of q_s.

7. Discussion of results and comparison with experiment

XPRs and marfes are two interrelated phenomena with significant impact on tokamak reactor safety. In order to reveal the processes and parameters governing the two phenomena, reduced models were developed that reproduce the corresponding experimental observations. Here, the results are summarized and compared with experiment.

7.1. XPRs

The formation of an XPR was investigated by means of a power balance. Similar to previous works dealing with marfe occurrence in the vicinity of material surfaces [1, 4, 8–10, 51], the present approach employs a balance of heat conduction with losses due to atomic processes. This description refers to a plasma volume magnetically separated from the wall, and therefore starts at the relatively high electron temperatures typical of the edge of divertor tokamak plasmas with auxiliary heating.

It is found that the neutral deuterium density near the X-point plays a key role in the initial reduction of the X-point temperature T_X via ionization and charge-exchange energy losses. A stable high-temperature power balance solution is found where T_X is above the main impurity radiation peak. The formation of an XPR was identified with a loss of this solution, which lead to the formulation of the XPR access condition (12). When the XPR parameter X_A surpasses a threshold, a thermal collapse occurs and an XPR forms at temperatures in the 1 eV range, where emission of Balmer and NIII recombination line radiation is expected as spectroscopically observed on AUG [14].

From the parameter dependencies of X_A in (13) or (15), an XPR requires high upstream density and low upstream temperature or low heating power, and occurs preferentially at higher values of the safety factor q_s. This is in line with the experimental observation that XPRs occur close to the density limit. The key geometric factor is the high flux expansion f_{exp} above the X-point. The importance of magnetic flux expansion for marfes, as it occurs on the high-field side of tokamaks due to the Shafranov shift, has also been highlighted in studies at TEXTOR [52].

X_A is independent of the impurity species and its concentration. A certain impurity content is, however, required to generate a thermal collapse once T_X is sufficiently low. The key external parameter is neutral gas fuelling that, together with recycling, determines the neutral density near the X-point. Since fuelling also increases and decreases upstream density and temperature, respectively, it has multiple promoting effects.

The importance of a high upstream density is a robust observation for the formation of stable X-point marfes [7, 11], as the XPR is also called. The importance of neutral gas fuelling for XPR formation was reported from investigations of the density limit on the divertor tokamaks DIII-D [11] and AUG [12, 16] as well as from SOLPS simulations of the L-mode density limit on AUG [14]. Maingi *et al* [53] investigated the DIII-D density limit by switching on and off a divertor cryopump. Without pumping, density limit disruptions involved the migration of a divertor marfe from the SOL onto closed flux surfaces near the X-point, that equates to the formation of an XPR in present terms. This transition, and the following density limit, was avoided by activating divertor pumping providing direct evidence for the key role of neutral deuterium. In addition, they showed that marfe formation could be avoided by operation at lower safety factors [53] in agreement with our strong scaling $X_A \sim q_s^2$ (13). The effect of the neutral density was also highlighted in recent detachment studies on the TCV tokamak [54]. A modification of the divertor baffles led to an increase in the neutral pressure in the divertor accompanied by a decrease in the line-averaged plasma density at which detachment is achieved [54]. It should be noted that higher neutral density compensates a lower upstream density in the XPR access parameter (13). A marfe study in the limiter tokamak TEXTOR [55] with an analytical and a numerical model also concluded that neutral hydrogen, in its case from local recycling at the limiter, plays an important role in triggering a marfe. In contrast to the present analysis, the impurity radiation peak was found to play a minor role.

When the high temperature power balance solution is lost after sufficient decrease in T_X, the resulting thermal collapse will lead to a rapid transition of T_X to low values (cf figure 4).

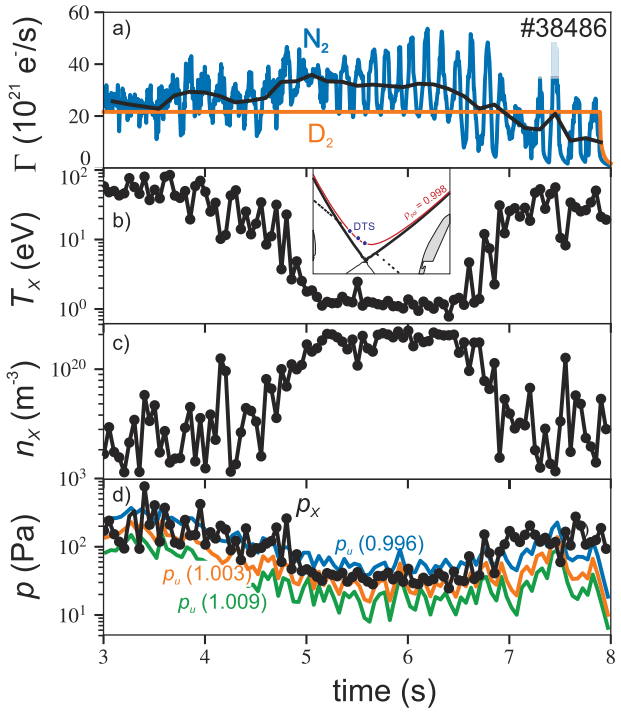

Figure 10. Temporal evolution of the electron temperature (*b*) and density (*c*) above the X-point as measured with the divertor Thomson scattering diagnostics on AUG and (*d*) the resulting electron pressure compared with the upstream pressure obtained from integrated data analysis for three values of the normalised plasma radius $\rho_{\rm pol}$ (in brackets). The dynamical evolution is caused by changes in the nitrogen fuelling rate (*a*) (black line is the 150 ms mean of the modulated flux in blue) at constant strong deuterium fuelling (in red). Thomson data are averages over three channels aligned on the flux surface at $\rho_{\rm pol} = 0.998$, as indicated in the insert in panel (*b*). For details of the discharge see [20].

Such an evolution of $T_{\rm X}$ was recently measured in detachment experiments on AUG [20] using the new divertor Thomson scattering diagnostics [56]. Figure 10 shows the evolution of the XPR plasma parameters induced by a variation of the nitrogen seeding rate in a discharge with strong deuterium fuelling. As discussed in section 4, at high neutral deuterium and nitrogen densities, the described process can also be driven by nitrogen. First $T_{\rm X}$ decreases gradually, as expected for the high-temperature solution, before it rapidly drops at about 4.8 s to 1–2 eV, probably due to a thermal collapse. At the same time the density rises to $n_{\rm X} \approx 2 \times 10^{20}$ m^{-3} while the kinetic electron pressure $p_{\rm X} = n_{\rm X} T_{\rm X}$ remains constant on the flux surface, as indicated by the comparison with the upstream kinetic pressure. This is as expected for a stable XPR solution.

The observed $T_{\rm X}$ dynamics is also reminiscent of the abrupt temperature drop at the outer strike point from $\geqslant$15 eV to $\leqslant$3 eV when the divertor detaches on DIII-D [57]. Since this process was only observed with a favorable ∇B drift direction, it was explained by means of the $E \times B$ drift. Nonetheless, it is noteworthy that [57] reports the upstream density at which the abrupt temperature drop occurs increases approximately as $\sqrt{P}$. Such a scaling is, instead, in agreement with (15) and (26), expressions for a critical density for XPR formation which yield $n_{\rm M}^{\rm (ii)} \sim P_{\rm sep}^{5/7}$.

Neutral deuterium is a recognized key player in the detachment of a divertor plasma (see e.g. [58, 59]). Although the present model was derived for a confined plasma volume, it may also be relevant in the initiation of divertor detachment, since in the SOL, laterally from the X-point, the flux expansion is also high. The TCV experiments [54], mentioned above, are an example of this. Recent SOLPS-ITER simulations for snow-flake divertor configurations highlighted the importance of the increased flux expansion in power dissipation and divertor detachment [60]. A strong temperature decrease in the X-point SOL region was able to trigger a strong influx of neutral particles into the XPR volume, which, in turn, lead to an XPR. Such a process may also be consistent with observations from the EAST tokamak. Equipped with a tungsten divertor, neon seeding was used in detachment experiments. An XPR (called X-point marfe) was observed when the cold detachment front in the SOL expanded from the divertor up to the X-point region [61].

The vertical extent of the XPR has not been addressed herein and a such description would necessitate an extension of this work. Qualitatively, its expansion could be understood as follows: the XPR first develops in a small volume just above the X-point, where the confined region flux expansion is strongest. Then, as the plasma becomes locally transparent to neutrals, the XPR extends further inwards. This process will cease as the upstream temperature, connected to the inner part of the growing XPR, will increase until the access condition (12) is no longer met. In this sense the XPR parameter $X_{\rm A}$ can be related to the size of the XPR volume. Mertens *et al* [7] reported, for carbon-wall AUG, that higher q_{95} and higher upstream densities let the XPR penetrate deeper into the plasma.

XPRs may be related in several ways to the enhanced transport and confinement degradation observed experimentally near the density limit [11, 12, 14, 16, 24, 62]. At high density, the upstream resistivity increases and a transition from drift-wave to interchange turbulence can occur as discussed in [63, 64]. This would reduce the temperature further and possibly trigger, from the strong temperature dependence of $X_{\rm A}$ (13), an XPR. Conversely, in a real plasma the heat dissipated from the XPR will reduce the upstream temperature and enhance the resistivity promoting the transition to enhanced interchange transport. These effects can be mutually reinforcing. It is interesting to note that the parameter dependence of the turbulence parameter [65, 66], which governs the transition to interchange turbulence, used in [64],

$$\alpha_{\rm t} \sim R_0 q_{\rm s}^2 \frac{n_{\rm u}}{T_{\rm u}^2},$$

bears strong similarity to the XPR parameter (13).

7.2. Marfes

The trigger for the marfe instability has been suggested to be the increase in the particle recombination rate above the level that can be compensated by parallel particle convection. The result is a pressure hole, being interchange unstable, that is advected toward the high-field side. The combined analysis

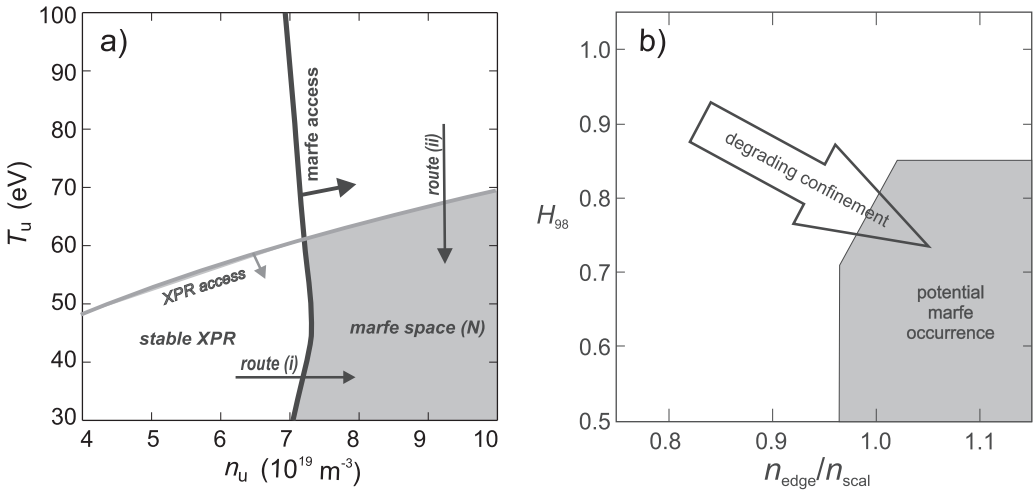

Figure 11. (*a*) Marfe map for nitrogen impurities from figure 9 with switched axes and (*b*) operational diagram based in figures 5 and 7 from reference [24] as function of a normalized edge density and the H-mode confinement factor H_{98}. The arrow indicates the evolution of H-mode discharges close to the density limit approaching the grey area where marfes are expected to occur.

of particle and power balances yielded the marfe parameter M_A (23), which, for high values, favors marfes, provided that an XPR has already formed. The two criteria for XPR access and stability were combined resulting in the marfe occurrence landscape of figure 9.

Here, two different possible routes to a marfe are indicated following different threshold density scalings. *Route (i)* starts from a plasma with an existing XPR. The critical density follows from M_A and scales as $n_M^{(i)} \sim 1/(q_s c_{imp}^{1/3})$ (see (24)). Along *route (ii)* the formation of an XPR leads inevitably to a marfe. The critical density now follows from the XPR parameter X_A scaling as $n_M^{(ii)} \sim P_{sep}^{5/7}/(n_0^{9/14} q_s^{4/9})$ (see (26)). In both cases, marfe formation is fostered by high safety factors and magnetic flux expansion. Large aspect ratio devices should have a stronger tendency to marfes than compact tokamaks. On route (i) the critical density is independent on the other plasma parameters, whereas on route (ii) the power crossing the separatrix and the neutral density can be used to actively prevent the plasma from generating a marfe.

Route (i) should describe experiments on early tokamaks with a carbon wall where the heating power was low. From figure 9, the carbon impurity produces marfes at relatively low density. Since, here, the edge temperature was also relatively low, an XPR could be present early on and the marfe would occur along route (i) during the density ramp. Experiments did, indeed, identify the density as the leading parameter for marfe formation [1, 4]. Their density threshold scaling is similar to that from our model: the original work on marfes [1] reports that the density threshold increases with plasma current $I_p \sim 1/q_s$ and decreases with the impurity concentration c_{imp}. A study on several tokamaks [4] resulted in a density threshold scaling $\sim 1/(q_s c_{imp}^{0.5})$ that is close to the model result (24) for $n_M^{(i)}$.

In tungsten devices with auxiliary heating, and e.g. nitrogen or argon seeding, the operational space for stable XPRs is wider (cf figure 9). Both routes are now available. Route (i) is appropriate when starting from a situation with a stable XPR. Here, a marfe can be triggered when passing the threshold $n_M^{(i)}$ during a density ramp. This would apply to L-mode plasmas, or H-mode plasmas where the edge temperature does not rise too high, due to core radiation or moderate heating. For strongly heated H-mode plasmas, route (ii) can occur where gas fuelling, or a drop in heating power, can trigger a marfe without forming an XPR. This would often lead to uncontrolled disruptions, as this process is too fast to take countermeasures. Increasing the neutral density shifts the vertical boundary in figure 9 to the right such that a plasma located at Ⓑ can also become unstable.

Finally, a few words about the marfe's dynamic. According to the model, a marfe should propagate in the high-field side direction. This is generally also observed in the experiment before a disruption occurs [7]. However, bolometric XPR observations show that the radiating zone first moves upward away from the X-point or toward the low-field side [19]. As discussed in section 5, however, this may be a consequence of the fact that the cold XPR core, where recombination occurs, must first grow, and thus shift the radiative front, before it can become unstable and move in high-field side direction.

7.3. Active marfe avoidance

Since marfes cause plasma disruptions that are incompatible with a fusion reactor, techniques for active disruption avoidance are being developed based on early marfe detection [24], where the penetration of a high-radiation zone into the confined plasma near the X-point is identified as the critical situation to avoid. On AUG, a plasma state map as function of a normalized edge density and the H-mode confinement factor H_{98} is used to determine when real-time control should intervene in the plasma discharge (see figures 5 and 7 in reference [24]). Figure 11(*b*) shows a sketch of this parameter map. The grey area covers the parameter space with a high potential for marfe occurrence and the arrow the typical locus of H-mode

discharges approaching the density limit with deteriorating confinement.

The operational diagram in figure 11(*b*) has the same structure as the marfe occurrence map from figure 9 with the axes switched such that the parameters become comparable, as in figure 11(*a*), where the upstream temperature relates to the confinement quality given by H_{98}. Active disruption avoidance aims to keep the plasma outside the parameter range indicated in grey by reducing the gas fuelling or increasing the heating power [24]. These two actuators are reminiscent of the critical density scaling of $n_{\mathrm{M}}^{(\mathrm{ii})}$ in (26). As discussed at the end of section 7.1, the XPR parameter (15), which yields the scaling of $n_{\mathrm{M}}^{(\mathrm{ii})}$, may also be pertinent to the extension of the XPR volume. For lower heating power and higher neutral deuterium density, the XPR can penetrate deeper into the plasma volume. For disruption avoidance, these parameter changes are reversed which has the desired effect of reducing the size of the XPR and avoid marfe occurrence which might need a certain volume to become unstable.

For safe plasma operation, it is recommended to enter the XPR regime at moderate densities and to actively control the XPR size through heating power and neutral gas fuelling. Entering the XPR regime at high edge density and edge temperature would more probably lead to uncontrollable disruptions along route (ii).

8. Conclusions

The active control of XPRs and marfes is important for a safe operation of future tokamak reactor plasmas. While an XPR is desirable for its contribution to power dissipation, to achieve stable divertor plasma detachment, marfes must be avoided as they can cause hazardous plasma disruptions. Despite their opposite effect on safe operation, the two phenomena are closely related. To identify their underlying processes and parameters, reduced models were developed, which reproduce many known experimental results. The main conclusions may be summarized from figure 9.

The formation of a stable XPR occurs at high values of the XPR parameter, that, according to (13) or (15), requires high neutral deuterium and edge plasma densities and a moderate edge electron temperature, respectively, low power crossing the separatrix. As external parameter, the neutral gas fuelling is most appropriate to trigger an XPR. The impurity species and its concentration do not enter the XPR parameter, but, at high concentrations, impurities can influence a transition through transport effects which were neglected herein. Although the model was developed for the confined plasma volume near the X-point, it may also apply to volumes in the SOL with high flux expansion and therefor help describe divertor detachment.

The formation of marfes, which are treated as unstable XPRs, can happen through two different routes. If an XPR is already present, marfes occur along route (i) (cf figure 9). This process only depends on the plasma edge density. The related critical density (24) scales inversely with safety factor and impurity concentrations in agreement with experiment. For safe plasma operation it is recommended to drive the plasma along this route and actively control the size of the XPR through heating power and neutral gas fuelling actuators.

In a plasma state at high edge density and temperature, where the XPR has not formed, an accidental reduction of the power crossing the separatrix or an increase in neutral gas fuelling can lead directly to an unstable marfe along route (ii) resulting in an uncontrollable disruption.

The model also describes why the threshold of a specific plasma state to the occurrence of marfes depends on the type of impurity. Carbon dominated plasmas are already able to develop marfes at low densities. At higher heating power, the plasma parameters take the fast and dangerous route (ii) when approaching the density limit. The parameter space for stable and controllable XPRs is wider in tungsten devices with nitrogen seeding and it increases further when argon is used. With neon seeding, the formation of a marfe is less likely for the parameters investigated. This shows that tungsten-wall devices, due to the freer choice of the impurity species for radiative cooling, have a higher flexibility for discharge control and safe plasma operation, than carbon-wall devices.

In the future, the main features of our model should be further verified experimentally on metal-wall devices such as AUG and JET. Thus, our model scalings may become a valuable resource for the scenarios development and active control schemes for stable divertor detachment and marfe avoidance for the safe operation of ITER and future reactors.

Acknowledgments

Useful discussions with the AUG marfe team, Anja Gude, Felix Klossek, Marc Maraschek and Bernhard Sieglin as well as with Peter Manz are gratefully acknowledged. A special thanks to Basil Duval for numerous helpful suggestions. This work has been carried out within the framework of the EUROfusion Consortium and has received funding from the Euratom research and training programme 2014–2018 and 2019–2020 under Grant Agreement No. 633053. The views and opinions expressed herein do not necessarily reflect those of the European Commission.

ORCID iDs

U. Stroth https://orcid.org/0000-0003-1104-2233
D. Brida https://orcid.org/0000-0002-8647-7058
T. Lunt https://orcid.org/0000-0002-7386-1456
O. Pan https://orcid.org/0000-0003-3827-0674

References

[1] Lipschultz B., LaBombard B., Marmar E.S., Pickrell M.M., Terry J.L., Watterson R. and Wolfe S.M. 1984 *Nucl. Fusion* **24** 977
[2] Alladio F. *et al* 1982 *Phys. Lett.* A **90** 405
[3] Baker D.R., Snider R.T. and Nagami M. 1982 *Nucl. Fusion* **22** 807
[4] Neuhauser J., Schneider W. and Wunderlich R. 1986 *Nucl. Fusion* **26** 1679

[5] Greenwald M. 2002 *Plasma Phys. Control. Fusion* **44** R27
[6] Murakami M., Callen J.D. and Berry L.A. 1976 *Nucl. Fusion* **16** 347
[7] Mertens V. *et al* 1994 *Plasma Phys. Control. Fusion* **36** 1307
[8] Ohyabu N. 1979 *Nucl. Fusion* **19** 1491
[9] Drake J.F. 1987 *Phys. Fluids* **30** 2429
[10] Borrass K., Campbell D.J., Clement S. and Vlases G.C. 1993 *Nucl. Fusion* **33** 63
[11] Petrie T. *et al* 1997 *J. Nucl. Mater.* **241–243** 639
[12] Potzel S., Wischmeier M., Bernert M., Dux R., Müller H.W. and Scarabosio A. 2013 *Nucl. Fusion* **54** 013001
[13] Nakano T., Kubo H., Asakura N., Shimizu K., Kawashima H. and Higashijima S. 2009 *J. Nucl. Mater.* **390–391** 255
[14] Reimold F., Wischmeier M., Bernert M., Potzel S., Kallenbach A., Müller H.W., Sieglin B. and Stroth U. 2015 *Nucl. Fusion* **55** 033004
[15] Field A.R. *et al* 2017 *Plasma Phys. Control. Fusion* **59** 095003
[16] Bernert M. *et al* 2017 *J. Nucl. Mater.* **12** 111
[17] Huber A. *et al* 2020 *Phys. Scr.* **T171** 014055
[18] Koubiti M. *et al* 2013 *J. Nucl. Mater.* **438** S559
[19] Bernert M. *et al* 2021 Control of the X-point radiator in fully-detached ASDEX-Upgrade H-mode plasmas *2020 IAEA Fusion Energy Conf.* (Nice 2021) (Vienna: IAEA) p EX/7–3 (https://conferences.iaea.org/event/214/contributions/17849/)
[20] Cavedon M *et al* 2022 *Nucl. Fusion* **62** 066027
[21] Loarte A. *et al* 1998 *Nucl. Fusion* **38** 331
[22] Wiesen S. *et al* 2015 *J. Nucl. Mater.* **463** 480
[23] Senichenkov I.Y., Kaveeva E.G., Rozhansky V.A., Voskoboynikov S.P., Veselova I.Y., Shtyrkhunov N.V., Coster D.P. and Bonnin X. 2021 *Plasma Phys. Control. Fusion* **63** 055011
[24] Maraschek M. *et al* 2018 *Plasma Phys. Control. Fusion* **60** 014047
[25] Lengyel L.L. 1988 *IPP Report 5/98* (Garching, Germany: Max-Planck-Institut für Plasmaphysik) unpublished
[26] Kallenbach A. *et al* 2013 *Plasma Phys. Control. Fusion* **55** 124041
[27] Reinke M.L. 2017 *Nucl. Fusion* **57** 034004
[28] Stroth U. 2018 *Plasmaphysik, Phänomene, Grundlagen, Anwendungen* (Berlin: Springer)
[29] Pitcher C.S. and Stangeby P.C. 1997 *Plasma Phys. Control. Fusion* **39** 779
[30] Stangeby P.C. 2000 *The Plasma Boundary of Magnetic Fusion Devices* (*Plasma Physics Series*) (Bristol: Institute of Physics Publishing)
[31] ADAS—atomic data and analaysis structure (http://adas.ac.uk/)
[32] Lechte C., Stöber J. and Stroth U. 2002 *Phys. Plasmas* **9** 2839
[33] Lipschultz B., LaBombard B., Terry J.L., Boswell C. and Hutchinson I.H. 2007 *Fusion Sci. Technol.* **51** 369
[34] Paradela Pérez I. *et al* 2017 *Nucl. Mater. Eng.* **12** 181
[35] Stangeby P.C. 1993 *Nucl. Fusion* **33** 1695
[36] Tokar M.Z. 2002 *Phys. Plasmas* **9** 1646
[37] Kallenbach A. *et al* 21 *Nucl. Fusion* **51** 094012
[38] Ryutov D.D., Cohen R.H., Farmer W.A., Rognlien T.D. and Umansky M.V. 2014 *Phys. Scr.* **89** 088002
[39] Kukushkin A.S. and Krasheninnikov S.I. 2019 *Plasma Phys. Control. Fusion* **61** 074001
[40] Post D.E. 1995 *J. Nucl. Mater.* **220–222** 143
[41] Carolan P.G. and Piotrowicz V.A. 1983 *Plasma Phys.* **25** 1065
[42] Dux R., Cavedon M., Kallenbach A., McDermott R.M. and Vogel G. (the ASDEX Upgrade Team) 2020 *Nucl. Fusion* **60** 126039
[43] Pan O. *et al* SOLPS-ITER simulations of X-point radiators in ASDEX Upgrade in preparation
[44] Neuhauser J., Braams B., Krech M., Ritschel U., Schneider W. and Wunderlich R. 1990 *Contrib. Plasma Phys.* **30** 95
[45] Stangeby P.C. 1991 *Plasma Phys. Control. Fusion* **33** 677
[46] Marchuk O. and Tokar M.Z. 2007 *J. Comput. Phys.* **227** 1597
[47] Ghendrih P. *et al* 2011 *Plasma Phys. Control. Fusion* **53** 054019
[48] Parks P.B., Sessions W.D. and Baylor L.R. 2000 *Phys. Plasmas* **7** 2968
[49] Krasheninnikov S.I., D'Ippolito D.A. and Myra J.R. 2008 *J. Plasma Phys.* **74** 679
[50] Bernert M. *et al* 2015 *Plasma Phys. Control. Fusion* **57** 014038
[51] de Vries P.C., Rapp J., Schüller F.C. and Tokar' M.Z. 1998 *Phys. Rev. Lett.* **80** 3519
[52] Tokar M.Z. 2001 *Phys. Plasmas* **8** 2866
[53] Maingi R. *et al* 1997 *Phys. Plasmas* **4** 1752
[54] Reimerdes H. *et al* 2021 *Nucl. Fusion* **61** 024002
[55] Tokar M.Z., Rapp J., Reiser D., Samm U., Schüller F.C., Sergienko G. and de Vries P.C. 1999 *J. Nucl. Mater.* **266–269** 958
[56] Design and first results of the new divertor Thomson scattering diagnostic on ASDEX Upgrade 2019 *Proc. of the 47th EPS Plasma Physics Conf.* Virtual
[57] McLean A. *et al* 2015 *J. Nucl. Mater.* **463** 533
[58] Krasheninnikov S.I., Kukushkin A.S. and Pshenov A.A. 2016 *Phys. Plasmas* **23** 055602
[59] Krasheninnikov S.I. and Kukushkin A.S. 2017 *J. Plasma Phys.* **83** 155830501
[60] Pan O., Lunt T., Wischmeier M., Coster D. and Stroth U. 2020 *Plasma Phys. Control. Fusion* **62** 045005
[61] Xu G. *et al* 2020 *Nucl. Fusion* **60** 086001
[62] Glöggler S. *et al* 2019 *Nucl. Fusion* **59** 126031
[63] Eich T., Manz P., Goldston R.J., Hennequin P., David P., Faitsch M., Kurzan B., Sieglin B. and Wolfrum E. 2020 *Nucl. Fusion* **60** 056016
[64] Eich T. and Manz P. (the ASDEX Upgrade Team) 2021 *Nucl. Fusion* **61** 086017
[65] Rogers B.N., Drake J.F. and Zeiler A. 1998 *Phys. Rev. Lett.* **81** 4396
[66] Scott B.D. 2005 *Phys. Plasmas* **12** 062314